

CLOSED LOOP CONTROL OF BIDIRECTIONAL BUCK-BOOST CONVERTER IN A SMART GRID USING PHOTOVOLTAIC AND ENERGY STORAGE SYSTEMS

¹Mr. K. Vijaya Kumar, ²Mrs. B. Sindhuja, ³Rudru Vijayalakshmi, ⁴Pullagura Tharani

^{1,3}Assistant Professor, ²Professor, ⁴Student

Department Of EEE

Gouthami Institute Of Technology & Management For Women, Proddatur, Ysr Kadapa, A.P

ABSTRACT—This paper proposes a new Closed loop control bidirectional buck-boost converter, which is a key component in a photovoltaic and energy storage system (PV-ESS). Conventional bidirectional buck-boost converters for ESSs operate in discontinuous conduction mode (DCM) to achieve zero-voltage-switching turn-on for switches. However, operation in DCM causes high ripples in the output voltage and current, as well as low power-conversion efficiency. To improve on the performance of the conventional converter, the proposed converter has a new combined structure of a cascaded buck-boost converter and an auxiliary capacitor. The combined structure of the proposed converter reduces the output current ripple by providing a current path and the efficiency is increased. The proposed Closed loop control converter has a maximum efficiency of 98%, less than 5.14 Vp.p of output voltage ripple, and less than 7.12 Ap.p of output current ripple. These results were obtained at an input voltage of 160 V, switching frequency of 45 kHz, output voltage of 80 ~ 320 V, and output power of 16 ~ 160 W. The experimental results show that the proposed converter has improved performance compared to the conventional converter.

Index Terms—DC-DC power conversion, Energy storage, Pulse width modulated power converters

1. INTRODUCTION

SMART grid (Fig. 1) is future electric energy system that has been studied to reduce mismatching between sources of electricity (such as renewable energy and power plants) and electricity consumers (homes, vehicles, factories, etc.). However, the energy production of renewable energy depends on environmental conditions. Therefore, an energy storage system (ESS) is needed in a smart grid to provide stability and efficiently manage the renewable energy [1-3]. An ESS consists of a battery that stores electric energy and a bidirectional

DC-DC converter that transfers energy from the battery and renewable energy source in both directions [4-9].

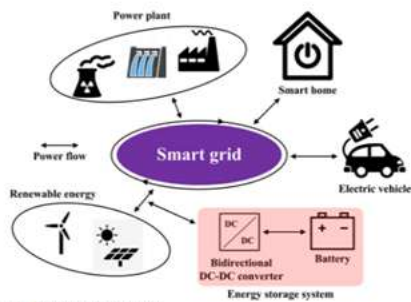
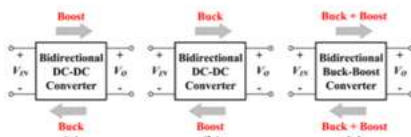


Fig. 1. Diagram of smart grid.

Fig. 2. Block diagrams in case of (a) $V_{IN} < V_O$, (b) $V_{IN} > V_O$, and (c) $V_{IN} < V_O$ & $V_{IN} > V_O$.

A conventional bidirectional DC-DC converter uses a half-bridge converter with two switches based on a buck or boost DC-DC converter. In the buck mode of the converter, electric energy is transferred from a high voltage (HV) port to the low voltage (LV) port. In boost mode, the electric energy is transferred from the LV port to the HV port. The conventional bidirectional converter has a limitation in that it can only be operated in buck mode in one direction and boost mode in the other direction (Fig. 2(a) and Fig. 2(b)) [10-12]. Therefore, when the input is a photovoltaic (PV) module and the output is battery cells in a smart grid, a half bridge converter based on a buck or boost converter cannot be used because of the following reasons: 1) The battery cells repeatedly perform charging and discharging operations, resulting in large voltage variation [13, 14]. 2) The PV module has a large voltage variation that depends on the module temperature and the solar irradiance [15-17]. Thus, the ranges of the input voltage and output voltage can overlap [18, 19].

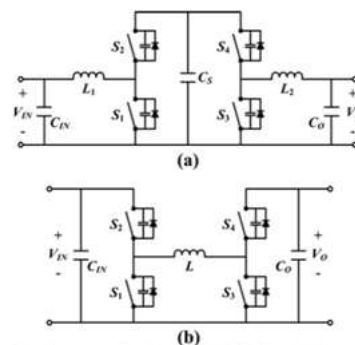


Fig. 3. Circuit structures of (a) Combined Half-Bridge (CHB) converter and (b) Cascaded Buck-Boost (CBB) converter.

Bidirectional buck-boost converters (Fig. 2(c)) were introduced for use in cases of overlapping input and output voltages [19-28]. They can operate in both buck and boost modes in both directions. A combined half-bridge (CHB) converter (Fig. 3(a)) is the most basic bidirectional buck-boost converter and has a symmetric structure with respect to the storage capacitor C_S [20, 21]. There is one inductor at the input port and one at the output port, which results in low voltage ripples in the input and output. However, because the CHB converter uses two inductors of the same size, it is large and has a low power-conversion efficiency η_e due to the DC-offset current of each inductor. Cascaded buck-boost (CBB) converter (Fig. 3(b)), along with the CHB converter, has been commonly used in ESSs. Compared with the CHB converter, CBB converter is smaller and has higher η_e because it uses only one inductor L [19, 22-28]. Recently, research has been actively conducted on bidirectional buck-boost DC-DC converters in discontinuous conduction mode (DCM) because this mode can achieve zero-voltage-switching (ZVS) turn-on of the switches [19, 26-28]. However, operation in DCM increases the current ripple of L , which affects the output current ripple and

increases the output voltage ripple. In this paper, an enhanced CBB converter is proposed to improve on the performance of the conventional CBB converter. The proposed converter is targeted to a PV-ESS system that uses a micro-inverter, which has been widely used in a smart grid [29, 30]. The converter has a new combined structure of a CBB converter and an auxiliary capacitor. This structure can reduce the output voltage ripple and increase η by effectively reducing the output current ripple.

II. DC-DC CONVERTERS

A DC-DC converter with a high step-up voltage, which can be used in various applications like automobile headlights, fuel cell energy conversion systems, solar-cell energy conversion systems and battery backup systems for uninterruptable power supplies. Theoretically, a dc-dc boost converter can attain a high step-up voltage with a high effective duty ratio. But, in practical, the step-up voltage gain is restricted by the effect of power switches and the equivalent series resistance (ESR) of inductors and capacitors.

Generally a conventional boost converter is used to get a high-step-up voltage gain with a large duty ratio. But, the efficiency and the voltage gain are restricted due to the losses of power switches and diodes, the equivalent series resistance of inductors and capacitors and the reverse recovery problem of diodes. Due to the leakage inductance of the transformer, high voltage stress and power dissipation effected by the active switch of these converters. To reduce the Voltage spike, a resistor-

capacitor –diode snubbed can be employed to limit the voltage stress on the active switch. But, these results in reduction of efficiency. Based on the coupled inductor; converters with low input ripple current are developed. The low input current ripple of these converters is realized by using an additional LC circuit with a coupled inductor.

III. PROJECT DESCRIPTION AND CONTROL DESIGN

PROPOSED DC-DC CONVERTER

A. Circuit Structure

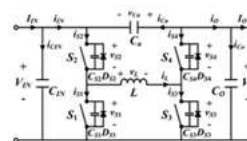


Fig. 4. Circuit structure of the proposed converter.

Six operating conditions	Types of the operation	Switches			
Directions of energy transfer		S_1	S_2	S_3	S_4
$V_o \rightarrow V_{in}$	Back	1-D	D	0	1
	Back-Boost	1-D	D	D	1-D
	Boost	0	1	D	1-D
$V_{in} \rightarrow V_o$	Back	0	1	D	1-D
	Back-Boost	1-D	D	D	1-D
	Boost	1-D	D	0	1

The proposed converter (Fig. 4) consists of a conventional CBB converter and an auxiliary capacitor (Ca), and has a symmetric structure with respect to Ca and L. The CBB converter consists of two capacitors (CIN, CO), four switches (S1, S2, S3, S4), and an inductor (L). Four switches (S1, S2, S3, S4) and an inductor (L) control the direction of energy transfer and the ratio between the input voltage and output voltage. Four switches are turned on in the ZVS condition by operating in DCM. Two capacitors (CIN, CO) reduce the output voltage ripple and noise, and an auxiliary capacitor (Ca) reduces the output current ripple by providing a current path.

B. Principle of Operation

The proposed converter operates with a fixed switching period T_S and controls the voltage gain by changing the duty ratio D of the switches (S1, S2, S3, S4) from 0 to 1. Each switch has four states in six operating conditions created by the energy transfer directions between V_{IN} and V_O and the types of operation (buck, boost, and buck-boost), as shown in Table I. Due to the symmetric structure with respect to C_a and L , the operations are separated by only the types of operation in one direction of energy transfer ($V_{IN} \rightarrow V_O$).

To simplify the analysis of the operation, the following assumptions are made: 1) the inductor and all capacitors are lossless, 2) the voltage ripples of C_{IN} , C_a , and C_O are small enough to assume that V_{IN} , V_{Ca} , and V_O are constant voltage sources, and 3) the converter operates in steady state.

(1) Buck mode When the proposed converter operates in buck mode, it has four distinct operating modes (Mode 1 ~ 4). The equivalent circuits and operating waveforms are shown in Fig. 5 and Fig. 6.

Mode 1 (Fig. 5(a), $t_0 \leq t \leq t_1$) starts when S2 is turned on. At $t = t_0$, S2 achieves ZVS turn-on because the body diode DS2 of S2 is turned on before $t = t_0$. Then, the voltage v_L of L becomes $V_{IN} - V_O$, and the current i_L of L is expressed as

$$i_L(t) = i_L(t_0) + \frac{V_{IN} - V_O}{L}(t - t_0). \quad (1)$$

The current i_{S2} of S2 is equal to i_L , so i_{S2} is expressed as

$$i_{S2}(t) = i_L(t_0) + \frac{V_{IN} - V_O}{L}(t - t_0).$$

In this mode, the current i_{Ca} of C_a , the current i_{Co} of C_O , the output current i_O , and the load current I_O have the following relations: $i_O = i_{Co} + I_O$, $i_{Co} = i_{Ca} \cdot C_O/C_a$,

and $i_O = i_L - i_{Ca}$. Therefore, i_{Ca} and i_O can be derived as

$$i_{Ca}(t) = \frac{C_a}{C_a + C_O} [i_L(t) - I_O]$$

$$i_O(t) = \frac{C_O}{C_a + C_O} i_L(t) + \frac{C_a}{C_a + C_O} I_O. \quad (2)$$

The voltage v_{Ca} across the auxiliary capacitor C_a is expressed as $v_{Ca}(t) = V_{Ca} + \Delta v_{Ca,AC}(t)$ where V_{Ca} and $\Delta v_{Ca,AC}$ represent the DC voltage and the AC ripple voltage across the C_a , respectively. Because $V_{Ca} \gg \Delta v_{Ca,AC}$, v_{Ca} can be approximated as $v_{Ca}(t) \approx V_{Ca} = V_O - V_{IN}$.

Mode 2 (Fig. 5(b), $t_1 \leq t \leq t_2$) starts when S2 is turned off. At this time, S1 remains in the off state to prevent a shoot-through problem with S1 and S2. In this mode, the output capacitor C_{S1} of S1 discharges from V_{IN} to 0, and the output capacitor C_{S2} of S2 charges from 0 to V_{IN} . Shortly after the discharging of C_{S1} and charging of C_{S2} are finished, the body diode DS1 of S1 is turned on. Mode 3 (Fig. 5(c), $t_2 \leq t \leq t_3$) starts with the ZVS turn-on of S1 because DS1 is turned on before $t = t_2$. Then, v_L becomes $-V_O$, and thereby i_L is expressed as

$$i_L(t) = i_L(t_2) - \frac{V_O}{L}(t - t_2). \quad (3)$$

Because $i_O = i_L - i_{Ca}$, $i_O = i_{Co} + I_O$, and $i_{Co} = i_{Ca} \cdot C_O/C_a$, i_{Ca} and i_O are expressed as

The current i_{S1} of S1 is equal to $-i_L$, so i_{S1} is obtained as

$$i_{S1}(t) = -i_L(t_2) + \frac{V_O}{L}(t - t_2).$$

Because $i_O = i_L - i_{Ca}$, $i_O = i_{Co} + I_O$, and $i_{Co} = i_{Ca} \cdot C_O/C_a$, i_{Ca} and i_O are expressed as

$$i_{Ca}(t) = \frac{C_a}{C_a + C_O} [i_L(t) - I_O] \quad (4)$$

$$i_O(t) = \frac{C_O}{C_a + C_O} i_L(t) + \frac{C_a}{C_a + C_O} I_O. \quad (5)$$

Mode 4 (Fig. 5(d), $t_3 \leq t \leq t_4$) starts when S1 is turned off and S2 remains in the off

state. In this mode, CS1 charges from 0 to VIN, and CS2 discharges from VIN to 0. Shortly after the charging of CS1 and discharging of CS2 are finished, DS2 is turned on. At t = t0, iL has an initial value of iL(t0), and iL(t0) is obtained as follows: By inserting t = t2 into (1), the current ripple ΔiL of iL is obtained as

$$\Delta i_L = i_L(t_2) - i_L(t_0) = \frac{V_{IN} - V_O}{L} D T_S, \quad (6)$$

where DTS = t2 - t0. The average current of L for one TS is obtained as = IO by applying the ampere-second balance law for capacitors to L () () () Ca Co += Itititi O . Then, iL(t0) = - ΔiL/2 is represented as

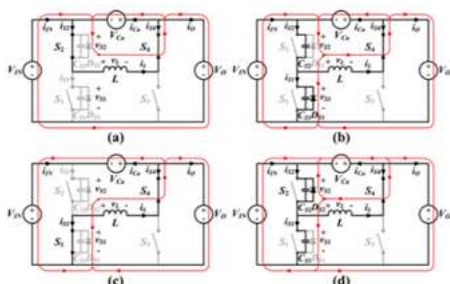


Fig. 5. Circuit diagrams for the operation of buck; (a) Mode 1, (b) Mode 2, (c) Mode 3, and (d) Mode 4.

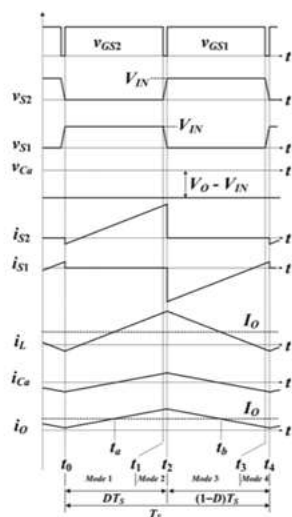


Fig. 6. Operational waveforms in the operation of buck.

$$i_L(t_0) = I_O - \frac{V_{IN} - V_O}{2L} D T_S, \quad (7)$$

and $i_L(t_2) = \langle i_L \rangle + \Delta i_L / 2$ is expressed as

$$i_L(t_2) = I_O + \frac{V_{IN} - V_O}{2L} D T_S. \quad (8)$$

(2) Boost mode

The boost operation also has four distinct operating modes (Mode 1 ~ 4), and the equivalent circuits and operating waveforms are shown in Fig. 7 and Fig. 8, respectively. Mode 1 (Fig. 7(a), t0 ≤ t ≤ t1) starts when S3 is turned on. At t = t0, S3 achieves ZVS turn-on because the body diode DS3 of S3 is turned on before t = t0. Then, vL becomes VIN, and iL is expressed as

$$i_L(t) = i_L(t_0) + \frac{V_{IN}}{L} (t - t_0). \quad (9)$$

The current iS3 of S3 is the same as iL, so iS3 is expressed as

$$i_{S3}(t) = i_L(t_0) + \frac{V_{IN}}{L} (t - t_0).$$

Because iO = -iCa, iO = iCo + IO, and iCo = iCa · CO/Ca, iCa and iO are expressed as

$$i_{Ca}(t) = -\frac{C_a}{C_a + C_O} I_O$$

$$i_O(t) = \frac{C_a}{C_a + C_O} I_O. \quad (10)$$

The voltage vCa across the auxiliary capacitor Ca is expressed as

$$v_{Ca}(t) = V_{Ca} + \Delta v_{Ca,AC}(t).$$

Because Ca Ca AC >> ΔvV , , this expression can be approximated as

$$v_{Ca}(t) \approx V_{Ca} = V_O - V_{IN}$$

Mode 2 (Fig. 7(b), t1 ≤ t ≤ t2) starts when S3 is turned off and S4 remains in the off state. In this mode, the output capacitor CS3 of S3 charges from 0 to VO, and the output capacitor CS4 of S4 discharges from VO to 0. Shortly after the charging of CS3 and discharging of CS4 are finished, the body diode DS4 of S4 is turned on. Mode 3 (Fig. 7(c), t2 ≤ t ≤ t3) starts with the ZVS turn-on of S4 because DS4 is turned on before t = t2. Then, vL becomes VIN - VO, and iL is expressed as

$$i_L(t) = i_L(t_2) + \frac{V_{IN} - V_O}{L} (t - t_2). \quad (11)$$

The current i_{S4} of $S4$ is equal to $-i_L$, so i_{S4} is obtained as

$$i_{S4}(t) = -i_L(t_2) - \frac{V_{IN} - V_O}{L}(t - t_2).$$

Because $i_O = i_L - i_{Ca}$, $i_O = i_{Co} + I_O$, and $i_{Co} = i_{Ca} \cdot CO/Ca$, i_{Ca} and i_O are expressed as

$$i_{Ca}(t) = \frac{C_a}{C_a + C_O} [i_L(t) - I_O] \quad (12)$$

$$i_O(t) = \frac{C_O}{C_a + C_O} i_L(t) + \frac{C_a}{C_a + C_O} I_O. \quad (13)$$

Mode 4 (Fig. 7(d), $t_3 \leq t \leq t_4$) starts when $S4$ is turned off and $S3$ remains in off-state. In this mode, $CS3$ discharges from V_O to 0 and $CS4$ charges from 0 to V_O . Shortly after the discharging of $CS3$ and charging of $CS4$ are finished, $DS3$ is turned on. By inserting $t = t_2$ into (9), Δi_L for boost operation is obtained as

$$\Delta i_L = i_L(t_2) - i_L(t_0) = \frac{V_{IN}}{L} DT_5, \quad (14)$$

where $DT_5 = t_2 - t_0$. Because $\langle i_L \rangle = I_{IN}$ and $i_L(t_0) = \langle i_L \rangle - \Delta i_L/2$, $i_L(t_0)$ is expressed as

$$i_L(t_0) = I_{IN} - \frac{V_{IN}}{2L} DT_5. \quad (15)$$

$i_L(t_2) = \langle i_L \rangle + \Delta i_L/2$ is expressed as

$$i_L(t_2) = I_{IN} + \frac{V_{IN}}{2L} DT_5. \quad (16)$$

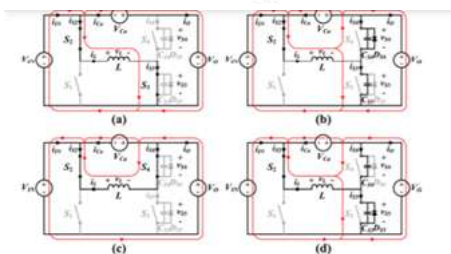


Fig. 7. Circuit diagrams for the operation of boost: (a) Mode 1, (b) Mode 2, (c) Mode 3, and (d) Mode 4.

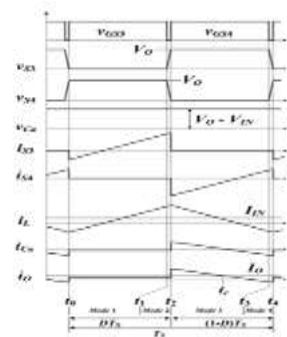


Fig. 8. Operational waveforms in the operation of boost.

waveforms are shown in Fig. 9 and Fig. 10, respectively. Mode 1 (Fig. 9(a), $t_0 \leq t \leq t_1$) starts when $S2$ and $S3$ are turned on. At $t = t_0$, $S2$ and $S3$ achieve ZVS turn-on because $DS2$ and $DS3$ are turned on before $t = t_0$. Then, v_L becomes V_{IN} , and i_L is expressed as

$$i_L(t) = i_L(t_0) + \frac{V_{IN}}{L}(t - t_0). \quad (17)$$

Both i_{S2} and i_{S3} are same as i_L , so they are expressed as

$$i_{S2}(t) = i_{S3}(t) = i_L(t_0) + \frac{V_{IN}}{L}(t - t_0).$$

Because $i_O = -i_{Ca}$, $i_O = i_{Co} + I_O$, and $i_{Co} = i_{Ca} \cdot CO/Ca$, i_{Ca} and i_O are expressed as

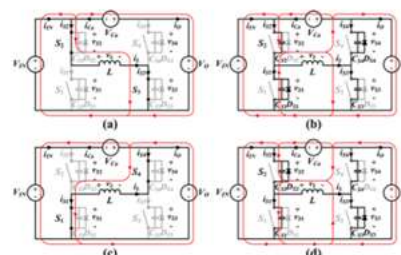


Fig. 9. Circuit diagrams for the operation of buck-boost: (a) Mode 1, (b) Mode 2, (c) Mode 3, and (d) Mode 4.

$$i_{Ca}(t) = -\frac{C_a}{C_a + C_O} I_O \quad (18)$$

$$i_O(t) = \frac{C_a}{C_a + C_O} I_O. \quad (19)$$

$v_{Ca}(t)$ is obtained using the equation (18) as

$$\begin{aligned} v_{Ca}(t) &= v_{Ca}(t_0) + \frac{1}{C_a} \int_{t_0}^t i_{Ca}(t) dt \approx v_{Ca} + \frac{1}{C_a} \left[\frac{-C_a I_O}{C_a + C_O} (t - t_0) \right] \\ &= V_O - V_{IN} - \frac{I_O}{C_a + C_O} (t - t_0). \end{aligned}$$

Mode 2 (Fig. 9(b), $t_1 \leq t \leq t_2$) starts when $S2$ and $S3$ are turned off and $S1$ and $S4$

remain in the off state. In this mode, CS2 and CS3 charge from 0 to VIN and from 0 to VO, respectively. CS1 and CS4 discharge from VIN to 0 and from VO to 0, respectively. Shortly after the charging and discharging processes are finished, the DS1 and DS4 are turned on. Mode 3 (Fig. 9(c), $t_2 \leq t \leq t_3$) starts with the ZVS turn-on of S1 and S4 because DS1 and DS4 are turned on before $t = t_2$. Then, vL becomes -VO, and iL is expressed as

$$i_L(t) = i_L(t_2) - \frac{V_O}{L}(t - t_2). \quad (20)$$

iS1 and iS4 are equal to -iL, so they are obtained as

$$i_{S1}(t) = i_{S4}(t) = -i_L(t) + \frac{V_O}{L}(t - t_2).$$

Because $i_O = i_L - i_{Ca}$, $i_O = i_{Co} + I_O$, and $i_{Co} = i_{Ca} \cdot CO/Ca$, i_{Ca} and i_O are expressed as

$$i_{Ca}(t) = \frac{C_a}{C_a + C_O} [i_L(t) - I_O] \quad (21)$$

$$i_O(t) = \frac{C_O}{C_a + C_O} i_L(t) + \frac{C_a}{C_a + C_O} I_O. \quad (22)$$

vCa is obtained using equations (20) and (21) as

$$v_{Ca}(t) = \frac{1}{C_a} \int_{t_2}^t i_{Ca}(t) dt + v_{Ca}(t_2) \\ = \frac{1}{C_a + C_O} \left[(i_L(t_2) - I_O)(t - t_2) - \frac{V_O}{2L}(t - t_2)^2 \right] + v_{Ca}(t_2).$$

Mode 4 (Fig. 9(d), $t_3 \leq t \leq t_4$) starts when S1 and S4 are turned off and S2 and S3 remain in the off state. In this mode, CS2 and CS3 discharge from VIN to 0 and from VO to 0, respectively. CS1

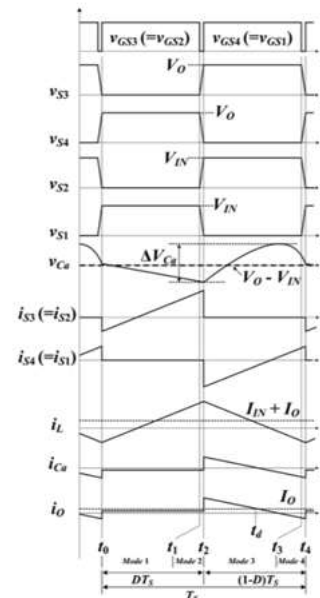


Fig. 10. Operational waveforms in the operation of buck-boost.

and CS4 charge from 0 to VIN and from 0 to VO, respectively. Shortly after the discharging and charging processes are finished, DS2 and DS3 are turned on. By inserting $t = t_2$ into (17), Δi_L is obtained for buck-boost operation as

$$\Delta i_L = i_L(t_2) - i_L(t_0) = \frac{V_{IN}}{L} D T_S, \quad (23)$$

where $D T_S = t_2 - t_0$. Because $i_L(t_0) = -\Delta i_L/2$, $i_L(t_0)$ is expressed as

$$i_L(t_0) = I_{IN} + I_O - \frac{V_{IN}}{2L} D T_S, \quad (24)$$

and $i_L(t_2) = +\Delta i_L/2$ is expressed as

$$i_L(t_2) = I_{IN} + I_O + \frac{V_{IN}}{2L} D T_S. \quad (25)$$

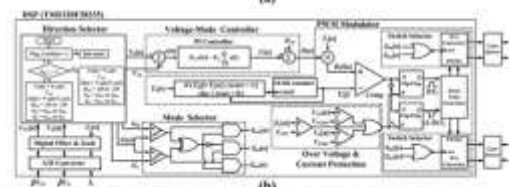
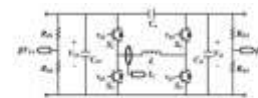


Fig. 11. (a) Circuit structure of the proposed converter with the voltage and current sensing (C_{Ca}, C_{Co}, and L), (b) Block Diagram of the digital controller for the proposed converter.

where $I_{C,rms}$ is the RMS value of the capacitor current, and RC is the ESR of the

capacitor. The voltages and currents of the key power components for calculating these power losses have different values for the different operating modes (Table II). The theoretical efficiency of the proposed converter can be calculated by inserting voltage and current values into the equations (43 ~ 49) related to the power loss calculations.

C. Operation of the Controller

The proposed converter is controlled by pulse width modulation (PWM) signals (vg1 ~ vg4), which are generated by the voltage-mode control (Fig. 11(a)). Two voltages (VIN and VO) are sensed to implement the voltage-mode control and protect the over voltage. VO is used as an output voltage for generating the PWM control signal of the main switch in the energy transfer direction from VIN to VO, and VIN is used as an output voltage in the opposite direction. The current of inductor is sensed to protect against over current.

Fig. 11(b) represents a block diagram of the digital controller for the proposed converter. When the energy transfer direction is expressed by the demand of the system, the direction selector determines the sensing output voltage (VIN or VO) needed for the voltage mode control. The voltage-mode PI controller then generates the duty ratio D of the main switch by comparing the sensed voltage with the reference voltage. The mode selector informs the PWM modulator of the operating mode of the proposed converter determined by the sensed VIN and VO. Finally, using the information from the mode selector and voltage mode controller, the PWM modulator and the switch

TABLE II
VOLTAGE AND CURRENT OF THE KEY POWER COMPONENTS FOR CALCULATING FIVE MAIN CAUSES OF POWER DISSIPATION

Five main causes of power dissipation	Operating modes		
	Buck mode	Boost mode	Buck-Boost mode
Switching loss of switch	$V_{S1,turn-off} = V_{S2,turn-off} = V_{IN}$ $I_{S1,turn-off} = -I_0 + \frac{V_{IN} - V_0}{2L} DT_S$ $I_{S2,turn-off} = I_0 + \frac{V_{IN} - V_0}{2L} DT_S$	$V_{S1,turn-off} = V_{S2,turn-off} = V_0$ $I_{S1,turn-off} = I_{IN} + \frac{V_{IN}}{2L} DT_S$ $I_{S2,turn-off} = -I_{IN} + \frac{V_{IN}}{2L} DT_S$	$V_{S1,turn-off} = V_{S2,turn-off} = V_{IN}$ $V_{S3,turn-off} = V_{S4,turn-off} = V_0$ $I_{S1,turn-off} = I_{S3,turn-off} = I_{IN} + I_0 + \frac{V_{IN}}{2L} DT_S$ $I_{S2,turn-off} = I_{S4,turn-off} = -I_{IN} - I_0 + \frac{V_{IN}}{2L} DT_S$
Conduction loss of switch	$I_{S1,con} = \sqrt{1-D} I_{L,con}$ $I_{S2,con} = \sqrt{D} I_{L,con}$ $I_{S3,con} = I_{L,con}$	$I_{S1,con} = \sqrt{D} I_{L,con}$ $I_{S2,con} = \sqrt{1-D} I_{L,con}$ $I_{S3,con} = I_{L,con}$	$I_{S1,con} = \sqrt{1-D} I_{L,con}$ $I_{S2,con} = \sqrt{D} I_{L,con}$ $I_{S3,con} = \sqrt{D} I_{L,con}$ $I_{S4,con} = \sqrt{1-D} I_{L,con}$
Winding loss of inductor	$I_{L,con}$ $= \sqrt{I_0^2 + \frac{V_{IN} - V_0}{2L} DT_S}$	$I_{L,con}$ $= \sqrt{I_{IN}^2 + \frac{V_{IN}}{2L} DT_S}$	$I_{L,con}$ $= \sqrt{(I_{IN} + I_0)^2 + \frac{V_{IN}}{2L} DT_S}$
Core loss of inductor	$M_L = \frac{V_{IN} - V_0}{L} DT_S$	$M_L = \frac{V_{IN}}{L} DT_S$	$M_L = \frac{V_{IN}}{L} DT_S$
ESR loss of capacitor	$I_{C1,con} = I_{C1,con}$ $= \frac{V_{IN} - V_0}{4\omega C_L} DT_S$	$I_{C2,con} = I_{C2,con}$ $= \frac{1}{2} \sqrt{1-D} I_{L,con}$	$I_{C3,con} = I_{C3,con}$ $= \frac{1}{2} \sqrt{1-D} I_{L,con}$

selector generates four gate signals (vg1 ~ vg4), which control the proposed converter.

IV. SIMULATION RESULTS

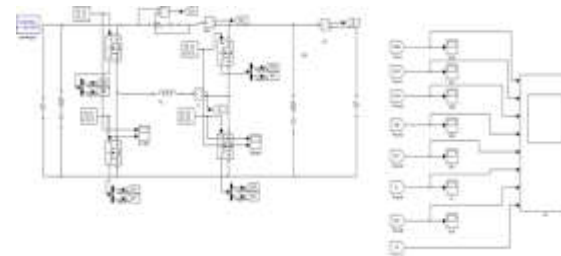


Fig: Circuit Diagram of BOOST Converter



Fig: Simulation Results for BOOST Converter

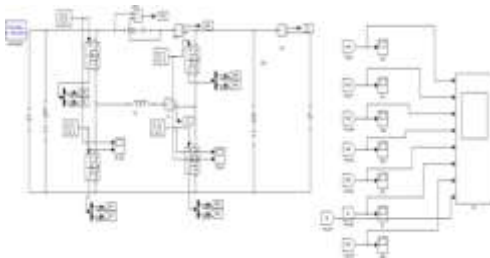


Fig: Circuit Diagram of BUCK Converter



Fig: Simulation Results for BUCK Converter

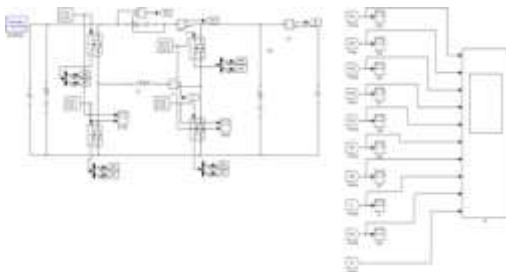


Fig: Circuit Diagram of BUCK-BOOST Converter

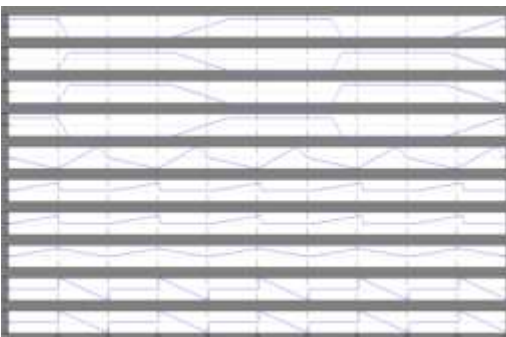


Fig.: Simulation Results for BUCK-BOOST Converter

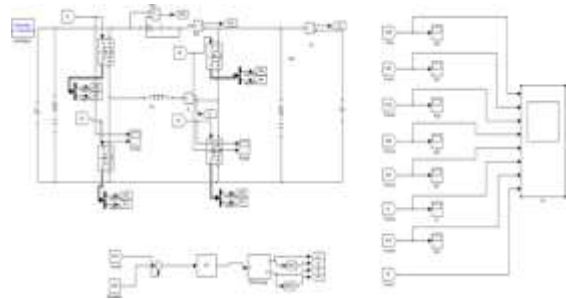


Fig.: Circuit Diagram of CLOSED BUCK Converter

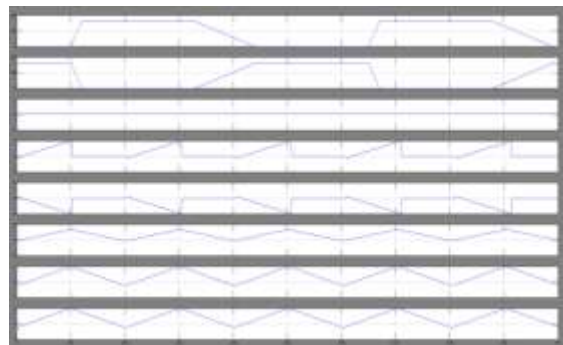


Fig.: Simulation Results for CLOSED BUCK Converter

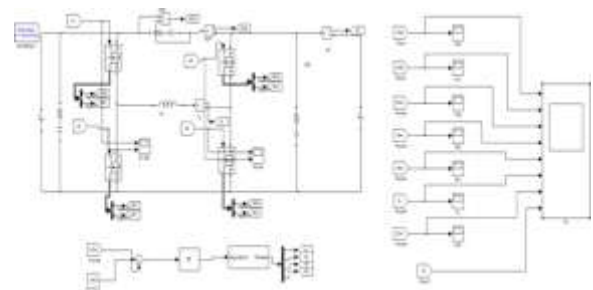


Fig.: Circuit Diagram of CLOSED BOOST Converter



Fig.: Simulation Results for CLOSED BOOST Converter

V.CONCLUSION

A new Closed loop control of bidirectional buck-boost converter was proposed in this paper. The proposed converter effectively had lower output current ripple than the conventional CBB converter, which was achieved by providing a bypass path for the output current. The reduced output current ripple enabled lower output voltage ripple and higher power-conversion efficiency compared to the conventional converter. The proposed converter had a maximum efficiency of 98% at $V_{IN} = 160$ V, $V_O = 80 \sim 320$ V, $P_O = 16 \sim 160$ W, and $f_S = 45$ kHz, and the output voltage ripple was less than 5.14 Vp.p. These results show that the proposed converter is suitable for PV-ESS in a smart grid, which requires a Closed loop control of bidirectional buck-boost converter with high efficiency and low ripples in the output voltage and current.

FUTURE SCOPE:

The Fuzzy based bidirectional buck-boost converter enhances the stability of the system and improves the dynamic response of the system operating in a better way and it has also effectively enhanced the damping

of bidirectional buck-boost converter simulation results.

REFERENCES

- [1] M. Sechilariu, W. Baochao, and F. Locment, "Building integrated photovoltaic system with energy storage and smart grid communication," *IEEE Trans. Ind. Electron.*, vol. 60, no. 4, pp. 1607–1618, Apr. 2013.
- [2] B. K. Bose, "Power electronics, smart grid, and renewable energy systems," in *Proc. IEEE*, vol. 105, no. 11, Nov. 2017.
- [3] L. Park, Y. Jang, S. Cho, and J. Kim, "Residential demand response for renewable energy resources in smart grid systems," *IEEE Trans. Ind. Informat.*, vol. 13, no. 6, pp. 3165–3173, Dec. 2017.
- [4] C. S. Lim and K. J. Lee, "Nonisolated two-phase bidirectional DC-DC converter with zero-voltage-transition for battery energy storage system," *Journal of Electrical Engineering & Technology*, vol. 12, no. 6, pp. 2237–2246, Nov. 2017.
- [5] M. Glavin, P. Chan, S. Armstrong, and W. Hurley, "A stand-alone photovoltaic supercapacitor battery hybrid energy storage system," in *Proc. 13th Power Electron. Motion Control Conf., 2008 (EPE-PEMC 2008)*, pp. 1688–1695.
- [6] J.-J. He, K.-W. Hu, and C.-M. Liaw, "On a Battery/Supercapacitor Powered SRM Drive for EV with Integrated On-board Charger," in *IEEE Industrial Technology Conference, Seville, 2015*.
- [7] S. H. Moon, S. T. Jou, and K. B. Lee, "Performance improvement of a bidirectional DC-DC converter for battery chargers using an LCLC filter," *Journal of*

Electrical Engineering & Technology, vol. 10, no. 2, pp. 742-755, Mar. 2015.

[8] Y. Du, X. Zhou, S. Bai, S. Lukic, and A. Huang, "Review of nonisolated bi-directional DC-DC converters for plug-in hybrid electric vehicle charge station application at municipal parking decks," in Proc. IEEE Appl. Power Electron. Conf., Feb. 2010, pp. 1145-1151.

[9] S. Vazquez, S. M. Lukic, E. Galvan, L. G. Franquelo, and J. M. Carrasco, "Energy storage system for transport and grid application," IEEE Trans. Ind. Electron., vol. 57, no. 12, pp. 3881-3895, Dec. 2010.

[10] M. Ahmadi, M. R. Mohammadi, E. Adib, and H. Farzanehfard, "Family of non-isolated zero current transition bi-directional converters with one auxiliary switch," IET Power Electron., vol. 5, no. 2, pp. 158-165, 2012.

[11] H.-L. Do, "Nonisolated bidirectional zero-voltage-switching DC-DC converter," IEEE Trans. Power Electron., vol. 26, no. 9, pp. 2563-2569, Sep. 2011.

[12] L. S. Yang and T. J. Liang, "Analysis and implementation of a novel bidirectional dc-dc converter," IEEE Trans. Ind. Electron., vol. 59, no. 1, pp. 422-434, Jan. 2012.

[13] O. Tremblay, L. Dessaint, and A. Dekkiche, "A generic battery model for the dynamic simulation of hybrid electric vehicles," in Proc. IEEE Vehicle Power Propuls. Conf., Sep. 2007, pp. 284-289.

[14] H. Wang, S. Dusmez, and A. Khaligh, "Design and analysis of a full bridge LLC based PEV charger optimized for wide battery voltage range," IEEE Trans. Veh. Technol., vol. 63, no. 4, pp. 1603-1613, Apr. 2014.

[15] B. Marion, "A method for modeling the current voltage curve of a PV module for outdoor conditions," Prog. Photovoltaic Res. Appl., vol. 10, no. 3, pp. 205-214, May 2002.